RSC Medicinal Chemistry

ROYAL SOCIETY OF CHEMISTRY

RESEARCH ARTICLE

Cite this: *RSC Med. Chem.*, 2022, **13**, 761

Copper chelating cyclic peptidomimetic inhibits Aβ fibrillogenesis†

Sujan Kalita, [a] Sourav Kalita, [a] Altaf Hussain Kawa,[a] Sukesh Shill,[a] Anjali Gupta,[b] Sachin Kumar[b] and Bhubaneswar Mandal *[a]

Misfolding of the amyloid-β peptide (Aβ) and its subsequent aggregation into toxic oligomers is one of the leading causes of Alzheimer's disease (AD). As a therapeutic approach, cyclic peptides have been modified in many ways and developed as a potential class of amyloid aggregation inhibitors. Head-to-tail cyclic peptides with alternating D, L amino acids inhibit amyloid aggregation significantly. On the other hand, excess deposition of copper, iron, and zinc enhances amyloid aggregation. Dysregulation of these metal ions in the brain triggers aggregation by binding to the Aβ peptide. Therefore, specific metal chelators have been developed for disrupting the Aβ-metal complex, thereby reducing toxicity and restoring metal ion homeostasis. Herein, we report the development of a head-to-tail cyclic peptidomimetic with a copper chelating ligand attached. The designed peptidomimetic inhibits amyloid aggregation significantly in a two-fold molar ratio to the Aβ peptide, as confirmed by the thioflavin T (ThT) fluorescence assay, dynamic light scattering (DLS), transmission electron microscopy (TEM), and Congo-red stained birefringence studies. The chelating ligand attached to the cyclic peptide binds efficiently to Cu^{2+} but weakly to Zn^{2+} and Fe^{2+}, thereby exhibiting profound selectivity, probed using UV-visible spectroscopy, thioflavin T (ThT) fluorescence assay, tyrosine (TYR10) fluorescence assay, isothermal titration calorimetry (ITC) and transmission electron microscopy (TEM). The non-toxicity of the designed peptidomimetics and their ability to reduce aggregating Aβ-fragment induced cytotoxicity was confirmed by the MTT assay on the mouse neuronal cell line. Further, the molecular interaction between the peptidomimetics and the Aβ-fragment was confirmed by Förster resonance energy transfer (FRET) studies using fluorescently labeled analogs. Cytotoxicity and cell internalization were also confirmed. A preliminary mechanistic investigation indicates that the peptidomimetic works by a synergistic effect of conformational restriction and metal sequestration. Such peptidomimetics can shed light on the mechanism of aggregation and a novel therapeutic approach.

Received 19th January 2022,
Accepted 9th May 2022

DOI: 10.1039/d2md00019a

rsc.li/medchem

Introduction

Alzheimer's disease (AD) is the most common dementia affecting the aged population.[1] AD is characterized by progressive memory impairment, impaired judgment, disordered cognitive behavior, depression, and confusion with time and space.[2] Under diseased conditions, natively unfolded Aβ peptides undergo a gradual conformational transformation from a monomeric state to toxic stable oligomeric aggregates rich in β-sheet conformation. Oligomers undergo further self-association into highly-ordered protofibrils, which, in the long run, self-assemble into well-organized mature amyloid fibrils.[3] Despite considerable efforts of the scientific research community, mechanistic insight into the process of amyloid aggregation remains enigmatic. No effective therapeutic agents have been clinically approved for treatment of such amyloidogenic disorders, despite consistent efforts devoted to understanding and clarifying the exact mechanism of protein aggregation and subsequent amyloid formation.[4]

AD is a complex and multifaceted disease that is not yet fully understood. However, one of the leading causes that contribute significantly to the progression of the disease is the aggregation of transmembrane peptides, called amyloid-β peptides ($Aβ_{1-40}$ and $Aβ_{1-42}$), produced by incorrect processing of amyloid precursor protein (APP).[3,5,6] Inhibitors of Aβ amyloidogenesis can be, therefore, potential drug candidates for the treatment or prevention of AD. Several inhibitors have been investigated to prevent or block amyloid

[a] *Laboratory of Peptide and Amyloid Research, Department of Chemistry, Indian Institute of Technology Guwahati, Assam-781039, India.*
E-mail: bmandal@iitg.ac.in
[b] *Department of Bioscience and Bioengineering, Indian Institute of Technology Guwahati, Assam-781039, India*

† Electronic supplementary information (ESI) available. See DOI: **https://doi.org/10.1039/d2md00019a**

fibrillation progression. Peptide-based Aβ aggregation modulators, such as KLVFF and LPFFD, are reported.[7,8] Peptide modification *via* incorporating an unnatural amino acid (anthranilic acid, Ant) exhibits profound inhibition of amyloid aggregation.[9] Despite the enormous successes in the growth of anti-AD agents, latent risks in safety issues and their bioavailability constitute a significant concern for their future development. Thus, naturally occurring compounds to combat AD are gaining considerable attention as therapeutic agents. Natural products such as polyphenols, flavonoids, tannins, saponins, alkaloids, and terpenes have exhibited crucial roles as inhibitors in neuropathological processes. To name a few, curcumin, resveratrol, epigallocatechin-3-gallate (EGCG), ginnalin A, brazilin, myricetin, sclerotiorin, and oleuropein have shown remarkable inhibitory efficacies against amyloid aggregation.[10–12] These natural compounds target and bind only to specific species generated during the amyloid aggregation pathway. Their precise mode of action is still unclear. However, it is likely to happen through multiple molecular mechanisms such as stabilising monomers, inhibiting proteins from getting misfolded, disrupting larger aggregates into smaller, stabilised species, and clearing misfolded proteins.[13,14] Many of these compounds have exhibited promising effects *in vitro* and *in vivo*, as they possess better pharmacological properties with lower toxicity and enhanced absorption efficiencies.[12] Natural product-based inhibitors have numerous beneficial effects. They have a high propensity to bind to misfolded proteins, possess diverse scaffolds, and exhibit enhanced safety and bioactivities, increased bioavailabilities, superior blood–brain-barrier (BBB) crossing abilities, free-radical scavenging, and anti-inflammatory properties.[11,14] Despite several beneficial aspects, they suffer from serious drawbacks, including poor solubility, rapid metabolism, detrimental side effects in clinical trials, and in a few cases, cytotoxicity.[13] Development of β-secretase and γ-secretase inhibitors is also a promising approach to tackle AD. β-Secretase inhibitors LY2886721, MK-8931, and E-2609 are under clinical trials.[15] Wood *et al.* reported sulfonamide based moieties as potential γ-secretase modulators that lower pathogenic Aβ levels by altering the enzyme cleaving site without hampering γ-secretase activity.[16]

On the other hand, cyclic peptides (CPs) have emerged as a potent class of amyloid aggregation inhibitors over the past few years. Cyclization of peptides exhibits several beneficial aspects; therefore, CPs are attractive drug candidates.[17–19] The majority of the clinically approved CPs have been derived from natural products, hormones, and antimicrobials.[20] *De novo* designed CPs sharing sequence homology with the Aβ peptide can bind to full-length Aβ and exhibit significant inhibition of amyloid fibrillogenesis. A pentapeptide fragment, KLVFF, corresponding to the Aβ16-20 region that serves as a self-recognizing moiety, plays a crucial role in manipulating amyloid fibrils.[21–23] Kanai *et al.* developed potent non-peptidic small molecule-based Aβ aggregation inhibitors considering cyclo-[KLVFF] as a lead peptide motif.[17] They further reported that the cyclic version of KLVFF (cyclo-[KLVFF] and its D-version cyclo-[klvff]) exhibited three times the inhibitory efficacy compared to linear KLVFF. Hence, the former can pave a promising route for establishing even more potent amyloid aggregation inhibitors. A more efficient inhibitor was developed by side-chain modification of cyclic KLVFF by incorporating an additional phenyl group at the β position of the Phe4 side chain, which produced less-toxic off-pathway oligomeric species with lower β-sheet content than the native oligomers.[18] Kapurniotu *et al.* introduced conformational restriction into a native amyloidogenic sequence *via* side chain-to-side chain cyclization, which confers non-amyloidogenicity to the sequence and interferes with Aβ amyloidogenesis.[24]

Molecules with enhanced flexibility have easy access to multiple conformational states. On the other hand, macrocyclic molecules are conformationally locked, which imparts constraints on their structural orientations. Cyclic peptides with 6, 10, and 14 α-amino acid residues have been reported to exhibit high β-sheet content, whereas macrocycles with 8, 12, and 16 residues exist mainly in random coil conformations.[25] Conformational restriction facilitates the binding of the macrocycle to the protein targets, enhancing the efficiencies of the macrocycles as inhibitors of aggregation. Richman *et al.* developed a cyclic alternating D,L-α-peptide as a potent amyloid inhibitor that interacts strongly with the Aβ peptide, inhibits its aggregation, disrupts the preformed fibrillar aggregates, and also protects rat cells from Aβ toxicity.[26]

In order to address the pathogenesis of AD and its mechanism of toxicity, several hypotheses have emerged, including the amyloid cascade hypothesis, tau hypothesis, toxic oligomer hypothesis, metal ion hypothesis, and oxidative stress hypothesis. Among them, the leading and the most widely accepted to date is the amyloid cascade hypothesis. This hypothesis suggests that the progression of AD is associated with the key events of excess production of Aβ, its aggregation, and simultaneous deposition in the brain as senile plaques, initiating a series of crucial events which eventually lead to AD dementia.[3,27] Numerous therapeutics reported to reduce Aβ production or aggregation have failed in phase III clinical trials, while others are in various stages of development. On the other hand, the toxic oligomer hypothesis indicates that the soluble Aβ oligomers are more toxic than the mature amyloid fibrils. These are the key etiologic agents in AD.[28] These soluble oligomeric species of Aβ are potent neurotoxins that deteriorate synaptic neurotransmission, mediate neuronal stress and oxidative damage, and lead to neuronal death in the long run.[29] The popular amyloid hypothesis suggests that membrane damage occurs due to fibrillization on the membrane surface, following a detergent-like mechanism, without considering the formation of pores; however, the toxic oligomer hypothesis suggests that the soluble oligomers cause membrane damage *via* ion-channel-like pores, excluding

fibrillization.[30] A general molecular model that includes both the amyloid and toxic oligomer hypotheses is the lipid-chaperone hypothesis, identified as a unique framework for protein-membrane poration. Due to their hydrophobic nature, lipids require chaperones, namely proteins, that bind to lipids for their trafficking in an aqueous environment in cells and cellular compartments.[31] Sciacca *et al.* demonstrated the crucial role of free lipids in forming an amyloidogenic lipid–protein complex in an aqueous solution. This becomes a lipid bilayer due to the chemical equilibrium between self-assembled lipids and free lipids in the aqueous phase. Such complexes facilitate the insertion of amyloidogenic proteins into cellular membranes and serve as the leading factor in the membrane damage process.[30]

Among them, metal ion dyshomeostasis is also gaining considerably equal attention. The post-mortem analyses of senile plaques found in AD patients' brains indicated an abnormal accumulation of metal ions such as copper, iron, and zinc.[32] *In vitro* studies reveal that the elevated levels of these metal ions coordinate to the Aβ peptide in senile plaques in AD, accelerating its aggregation and toxicity.[33] Recent studies have indicated that the imbalance of these biometals plays a significant role in lipid peroxidation, protein oxidation, and DNA oxidation.[34] Metal stabilizes the oligomeric form of Aβ. Such Aβ-metal complexes catalyze dioxygen reduction in the presence of endogenous reductants, generating reduced reactive oxygen species (ROS) such as H_2O_2 *via* the Fenton cycle.[32] This causes increased oxidative stress and damage to cellular components like DNA, lipids, and proteins. Widespread oxidative damage in the brain and synaptic loss eventually leads to neuronal death.[15,35] Furthermore, a recent report revealed that Zn extraction from the Aβ aggregate accelerated its natural degradation by the insulin-degrading enzyme (IDE).[36]

Restoring metal homeostasis and preventing oxidative damage in the brain is a promising therapeutic strategy for treating AD. Hence, disruption of the Aβ-metal complex and sequestration of metal ions by specific metal chelators have been extensively explored. Many bifunctional and multifunctional metal chelators have been developed, having high specificity for respective metals, which can chelate metal ions from Aβ deposits, reduce metal-induced Aβ aggregation, increase antioxidant properties and increase blood–brain barrier crossing ability. Desferrioxamine B was the first metal chelator studied *in vivo*, followed by deferiprone and PBT2 derivatives.[3,37] The 8-hydroxyquinoline based moiety, clioquinol, a bidentate ligand, perturbs the metal-induced aggregation of Aβ *via* metal chelation.[38,39] Li *et al.* developed a series of multitarget-directed resveratrol derivatives that exhibited significant Aβ aggregation inhibition and proved to be effective antioxidants and metal chelators.[40] Mirica *et al.* designed novel bifunctional metal chelators based on the core structure of the amyloid-binding fluorescent dye thioflavin T (ThT). These metal chelators reduced the cell toxicity of preformed Aβ oligomers as well as copper-stabilized Aβ oligomers.[41] Certain 2-methylaminopyridine derivatives have been reported to chelate both Cu(II) and Zn(II) with a higher binding affinity for the former, giving rise to 1:1 and 1:2 metal–ligand complexes in both cases.[42] Pyridine-2-carboxylic acid or picolinic acid (**PA**) possesses efficient chelating properties and is an ideal metal-binding ligand, forming stable metal complexes with biologically essential metals such as copper, iron, and zinc.[43] The chelating property of **PA** was first reported by Weidel in 1879, chelating copper and iron efficiently.[44] It also stimulates programmed cell death in cancer cells and exhibits efficient interruption in the progress of HIV *in vitro*.[45] Based on the ability of **PA** to prevent cell growth and arrest the cell cycle, **PA**-based Cu(II) complexes have been designed that bind to DNA and cleave it. These complexes also function as DNA recognition elements and metal-based anticancer agents.[46]

Inspired by the chelating efficiency of **PA** and considering the diversity of cyclic peptides as inhibitors against amyloid fibrillogenesis, we herein report the design, synthesis, and characterization of head-to-tail cyclic peptides with (**PA^{19}fCP**) and without (**^{19}fCP**) incorporating **PA** (Fig. 1). The corresponding linear analog (**^{19}fLP**) was also prepared that served as a control. We have investigated the anti-amyloidogenic efficacy and metal chelating efficiency of **PA^{19}fCP** using different biophysical tools to investigate the synergistic effect of cyclization and metal chelation.

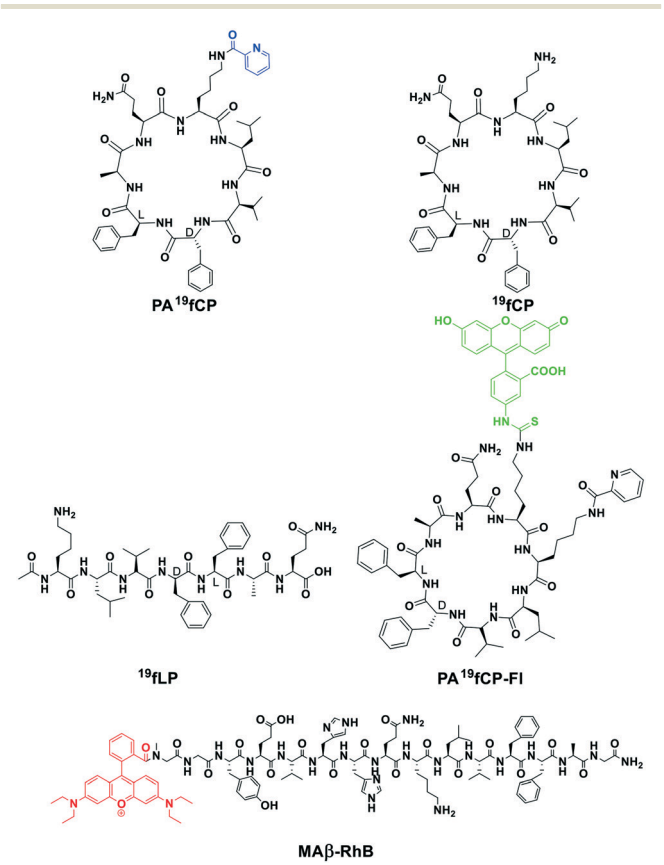

Fig. 1 Chemical structures of PA^{19}fCP, ^{19}fCP, ^{19}fLP, PA^{19}fCP-Fl, and MAβ-RhB.

Results and discussion

Peptide design and synthesis

A convenient strategy for synthesizing on-resin head-to-tail cyclic peptides by solid-phase peptide synthesis (SPPS) involves anchoring a trifunctional amino acid to the resin through its side-chain with orthogonal protection strategies, Fmoc/tBu/OAll.[47] Reported aggregation inhibiting head-to-tail cyclic peptides comprises all L-form or D-form or alternating D, L amino acids. To the best of our knowledge, no cyclic peptides with a single D-amino acid have yet been tested to inhibit Aβ fibrillogenesis. Replacement of L- with D-amino acids in a peptide increases its enzymatic stability and potency as an inhibitor against amyloid fibrillogenesis.[48] Incorporation of D-amino acids in a peptide is also beneficial as specific folded structures can be achieved due to their conformational preferences. Arai *et al.* performed a series of derivatizations of the cyclic version of KLVFF by replacing all L-amino acids with the corresponding D-amino acids and inserting a single L-amino acid in a sequence of all D-amino acids and investigated their inhibitory activities upon Aβ aggregation.[17] They developed pharmacophore motifs for Aβ aggregation inhibitors based on the structure–activity relationship studies of a vast library of peptides.

In contrast, our cyclic peptides (**CP**s) were designed in a way that included only one D-amino acid (D-phenylalanine) in a sequence of all L-amino acids, *i.e.*, KLVfFAE (**PA^{19}fCP**) (**E** converted to **Q** after cleavage from the resin. Detailed text on page S12 and S13, ESI†). Since it is common to place a turn-inducing element in the middle of a linear peptide sequence to facilitate cyclization, to achieve our target, we have inserted the D-phenylalanine precisely in the middle of the sequence. Moreover, it was demonstrated through alanine substitution that Phe20 is crucial for binding to Aβ and inhibition of Aβ fibril formation.[7] Hence, we maintained the sequence so that Phe20 remained intact and inserted the D-phenylalanine in position 19 instead of 20. The synthesized peptides were characterized by RP-HPLC and mass spectrometry.

Inhibition of $A\beta_{1-40}$ aggregation by the CPs

We investigated the efficacy of the synthesized head-to-tail cyclic peptides (**PA^{19}fCP** and **^{19}fCP**) in arresting amyloid fibrils and inhibiting amyloid aggregation and compared the same with a linear control peptide (**^{19}fLP**). $A\beta_{1-40}$ (40 μM) was co-incubated in the absence and presence of 0.5-, 1- and 2-fold molar excesses of **PA^{19}fCP**, **^{19}fCP**, and **^{19}fLP** for six days in PBS pH 7.4, at 37 °C.

The kinetics of amyloid formation and aggregation inhibition by the synthesized peptides were monitored by a time-dependent thioflavin T (ThT) fluorescence assay. The conformational changes of the peptides were investigated by circular dichroism (CD) and Fourier transform infrared spectroscopy (FT-IR).

In the ThT experiment, the fluorescence intensity of $A\beta_{1-40}$ increased with time when incubated alone (black, Fig. 2(a) and (b)). But, in the presence of 0.5- (red, Fig. 2(a) and (b)), 1- (blue, Fig. 2(a) and (b)) and 2- (magenta, Fig. 2(a) and (b)) fold molar excesses of **PA^{19}fCP** and **^{19}fCP**, respectively, it decreased gradually in a dose-dependent manner. The fluorescence intensity decreased significantly with increasing doses of cyclic peptides, indicating inhibition of $A\beta_{1-40}$ aggregation. Similarly, when incubated alone, the

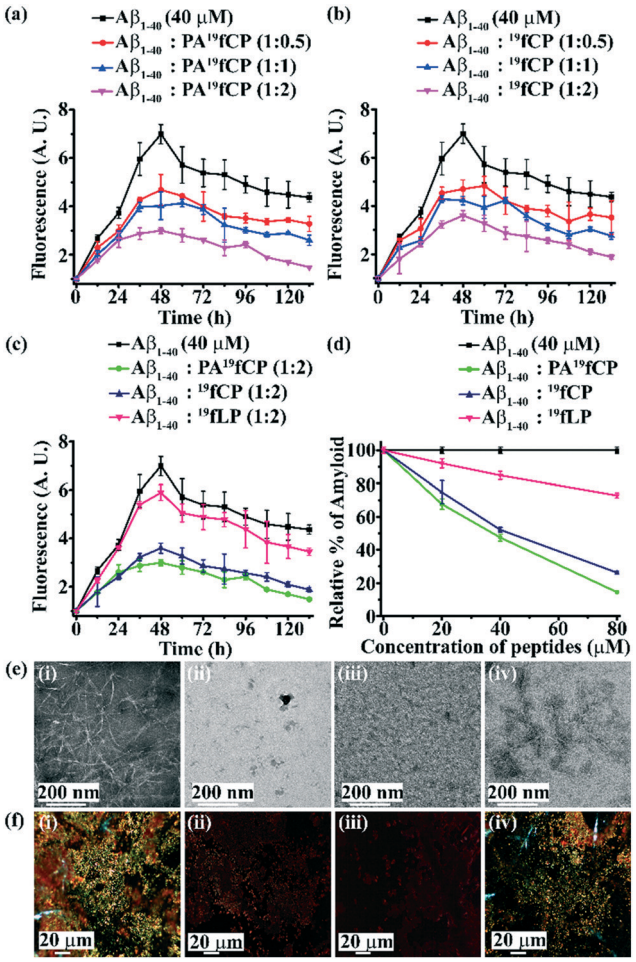

Fig. 2 (a) Time-dependent ThT fluorescence assay of $A\beta_{1-40}$ (40 μM) in the absence (black) and the presence of 0.5- (red), 1-(blue), and 2-(magenta) fold molar excesses of **PA^{19}fCP**, (b) time-dependent ThT fluorescence assay of $A\beta_{1-40}$ (40 μM) in the absence (black) and the presence of 0.5- (red), 1-(blue) and 2-(magenta) fold molar excesses of **^{19}fCP**, (c) time-dependent ThT fluorescence assay of $A\beta_{1-40}$ (40 μM) in the absence (black) and in the presence of 2-fold molar excesses of **PA^{19}fCP** (green), **^{19}fCP** (navy) and **^{19}fLP** (pink), and (d) dose-dependent ThT fluorescence assay of $A\beta_{1-40}$ (40 μM) in the absence (black) and the presence of various molar excesses of **PA^{19}fCP** (green), **^{19}fCP** (navy) and **^{19}fLP** (pink). The peptide solutions were incubated in PBS at pH 7.4 and 37 °C. (e) TEM and (f) Congo red-stained birefringence images of $A\beta_{1-40}$ in the absence (i) and in the presence of 2-fold molar excesses of (ii) **PA^{19}fCP**, (iii) **^{19}fCP**, and (iv) **^{19}fLP**. The scale bars for (e) and (f) are 200 nm and 20 μm, respectively (the images were captured after six days of incubation of the peptide samples in PBS at pH 7.4 and 37 °C. The ThT experiment was repeated thrice. All the results were consistent. For each solution, two sets were prepared, and three readings were recorded separately for each set. Each graph represents an average of six readings. Error bars indicate standard deviations).

fluorescence intensity of $A\beta_{1-40}$ was found to increase with time (black, Fig. 2c), but in the presence of 2-fold molar excesses of **PA^{19}fCP** (green, Fig. 2c) and **^{19}fCP** (navy blue, Fig. 2c), it was suppressed significantly, indicating the efficacies of the **CP**s to inhibit amyloid fibrillation. The 2-fold molar excess of the control peptide **^{19}fLP** also reduced the fluorescence intensity of $A\beta_{1-40}$, (pink, Fig. 2c), but to a much lesser extent than the **CP**s. Therefore, the **CP**s exhibited better inhibition potential than their linear precursor, **^{19}fLP**, implying the effect of cyclization upon inhibition of amyloid aggregation.

From the dose-dependent study, the percentage of amyloid inhibition by 0.5-, 1- and 2-fold molar excesses of **PA^{19}fCP** was observed to be 32.43%, 52.58%, and 85.56%, respectively (green, Fig. 2d), whereas the same for **^{19}fCP** was observed to be 25.24%, 47.88%, and 73.72%, respectively (navy blue, Fig. 2d). In contrast, the percentage of amyloid inhibition by 0.5-, 1- and 2-fold molar excesses of **^{19}fLP** was observed to be only 7.90%, 15.12%, and 27.21%, respectively (pink, Fig. 2d). Thus, two equivalents of the **CP**s exhibited much better inhibitory efficacy with a significant extent of inhibition than their linear precursor, **^{19}fLP**. Thus, we reconfirmed that the cyclic peptides are better at inhibiting amyloid aggregation than the linear analogs.

Further, the appearance of fibrillar assembly under transmission electron microscopy (TEM) and green-gold birefringence under cross-polarized light upon staining with Congo-red dye is a characteristic feature of amyloid formation.[49,50] $A\beta_{1-40}$ alone exhibited rich fibrillar morphology when observed under TEM (Fig. 2e (i)), indicating significant growth of amyloid fibrils. However, when $A\beta_{1-40}$ was co-incubated in the presence of 2-fold molar excesses of **PA^{19}fCP** (Fig. 2e (ii)) and **^{19}fCP** (Fig. 2e (iii)), and then TEM was recorded, such fibrillar assembly was not observed, indicating inhibition of amyloid aggregation. However, in the presence of 2-fold molar excess of **^{19}fLP** (Fig. 2e (iv)), $A\beta_{1-40}$ exhibited some fibrillar network under TEM, highlighting the inefficiency of 2 equivalents of **^{19}fLP** to inhibit aggregation to a significant mark. Therefore, although two equivalents of the **CP**s could perturb the fibrillar assembly, the same amount of **^{19}fLP** was not sufficient to accomplish the same. Similarly, when observed under cross-polarized light, $A\beta_{1-40}$ alone exhibited bright green-gold birefringence upon staining with Congo red dye (Fig. 2f (i)), indicating amyloid formation. But, when $A\beta_{1-40}$ was co-incubated in the presence of 2-fold molar excesses of **PA^{19}fCP** (Fig. 2f (ii)) and **^{19}fCP** (Fig. 2f (iii)), no such green-gold birefringence was observed, indicating inhibition of amyloid aggregation. However, in the presence of a 2-fold molar excess of **^{19}fLP**, some green-gold birefringence was observed (Fig. 2f (iv)), indicating the inability of 2 equivalents of **^{19}fLP** to inhibit $A\beta_{1-40}$ aggregation.

Further, after six days of incubation, $A\beta_{1-40}$ alone exhibited a β-sheet rich conformation both in CD and FT-IR analyses (black, Fig. S10(a) and (b), ESI†) but, in the presence of 2-fold molar excesses of **PA^{19}fCP** and **^{19}fCP** (red and blue, respectively, Fig. S10(a) and (b), ESI†), the β-sheet content was found to reduce, mainly exhibiting random coil conformations. Meanwhile, in the presence of 2-fold molar excess of **^{19}fLP**, a small amount of β-sheet conformation was observed (magenta, Fig. S10(a) and (b), ESI†). This observation further confirms the efficacies of the **CP**s in inhibition of aggregation compared to **^{19}fLP**. Results demonstrate the potential of **PA^{19}fCP** and **^{19}fCP** over **^{19}fLP** as efficient inhibitors of $A\beta_{1-40}$ aggregation, exhibiting significant inhibition of ~85% and 74%, respectively, even if with a two-fold molar ratio. In other words, head-to-tail cyclic peptides with a single D-amino acid inserted into their sequences proved to be better amyloid aggregation inhibitors than their linear precursors. Although the inhibitory efficacies of **PA^{19}fCP** and **^{19}fCP** were almost comparable, the former exhibited, to some extent, better inhibition of $A\beta_{1-40}$ aggregation compared to the latter, implying some hidden effects of the picolinic moiety upon aggregation inhibition.

Metal chelating efficacy of PA^{19}fCP probed by UV-visible spectroscopy

As mentioned previously, **PA^{19}fCP** was designed to perform the dual function of inhibition of amyloid aggregation and metal sequestration from the Aβ-metal complex. A potential metal chelator is expected to extract the metal ions from the Aβ-metal aggregates and reduce the fibril formation initiated by the metal-induced aggregation. Wu and coworkers reported that apocyclen attached to the central recognition motifs of Aβ could efficiently abstract copper from Aβ-Cu(II) complexes.[51] The proteolytically active complex thus formed was shown to interfere with Aβ aggregation, disaggregated the preformed Aβ fibrils, and prevented H_2O_2 generation and toxicity in living cells. In our study, the metal-chelation efficacy of picolinic acid (**PA**) attached to **PA^{19}fCP** towards copper, iron, and zinc was first investigated using UV-visible spectroscopy.[37] It was observed that the λ_{max} of **PA^{19}fCP** (black, Fig. 3(a) and (b)) in methanol changed in the presence of Cu^{2+} (red, Fig. 3(a) and (b)) and Zn^{2+} (magenta,

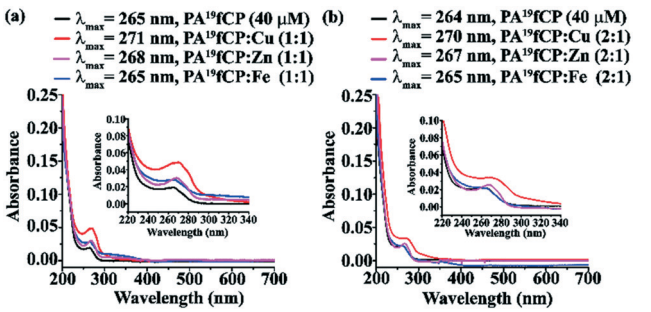

Fig. 3 (a) UV-visible spectra of **PA^{19}fCP** alone (black) and in the presence of 1 : 1 molar ratios of Cu^{2+} (red), Zn^{2+} (magenta) and Fe^{2+} (blue) ions. (b) UV-visible spectra of **PA^{19}fCP** alone (black) and in the presence of 2 : 1 molar ratios of Cu^{2+} (red), Zn^{2+} (magenta) and Fe^{2+} (blue) ions. The representative results out of several independent repeats are shown.

Fig. 3(a) and (b)) ions, but remained unchanged in the presence of Fe^{2+} ions (blue, Fig. 3(a) and (b)). Redshifts from 265 nm to 271 nm and from 264 nm to 270 nm upon adding **PA^{19}fCP** to $CuSO_4$ in 1 : 1 and 2 : 1 ratios, respectively, suggested metal-**PA^{19}fCP** complex formation in both cases.

Similarly, upon adding **PA^{19}fCP** to $ZnCl_2$ in 1 : 1 and 2 : 1 ratios, the λ_{max} shifted from 265 nm to 268 nm and 264 nm to 267 nm, respectively, forming metal-**PA^{19}fCP** complexes in both cases. However, upon addition of **PA^{19}fCP** to $FeSO_4$ in 1 : 1 and 2 : 1 ratios, hardly any significant difference was observed, indicating that **PA^{19}fCP** might not complex with Fe^{2+} ions or if at all it did, then, probably the complexation would be too weak to be detected in λ_{max} shift in the UV spectrum.

The maximum shift in wavelength was observed only for complexation with Cu^{2+} ions, whereas Zn^{2+} ions exhibited just a slight shift in wavelength. Therefore, **PA** in **PA^{19}fCP** exhibited selectivity in chelating these metal ions, having the highest chelating affinity for Cu^{2+} ions, followed by Zn^{2+} ions with insignificant or almost no affinity for Fe^{2+} ions.

Effects of PA^{19}fCP on metal-induced Aβ$_{1-40}$ aggregation monitored by the ThT assay

The influence of **PA^{19}fCP** on the inhibition of metal-induced $A\beta_{1-40}$ aggregation was monitored by the thioflavin T (ThT) fluorescence assay.[37] $A\beta_{1-40}$ (40 μM) was co-incubated with 40 μM each of $CuSO_4$, $FeSO_4$, and $ZnCl_2$, followed by the addition of **PA^{19}fCP** (80 μM) to these solutions separately. A blank sample was also prepared. All the samples were incubated at 37 °C in PBS at pH 7.4 for 36 h, fluorescence was recorded with an excitation wavelength (λ_{ex}) of 440 nm, and then emission (λ_{em}) was measured at 485 nm.

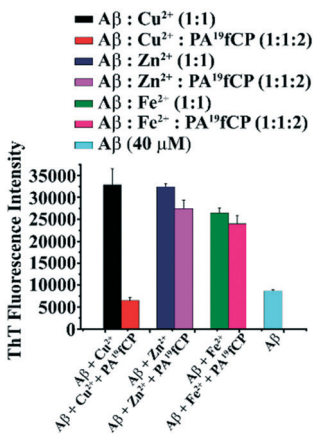

Fig. 4 ThT fluorescence assay of metal-induced $A\beta_{1-40}$ aggregation exhibiting the effect of **PA^{19}fCP** upon it. The ThT fluorescence intensities of the respective samples depicted in the above figure were obtained by subtraction from that of the reference, *i.e.* samples containing only ThT solution and PBS buffer. All the samples were incubated in PBS at 37 °C for 36 h ([$A\beta_{1-40}$] = 40 μM; [M^{2+}] = 40 μM; [**PA^{19}fCP**] = 80 μM, results are averages of three independent experiments, error bars indicate standard deviations).

From the ThT experiment, it was observed that $A\beta_{1-40}$ aggregation was much less for such a short incubation time (cyan, Fig. 4), but the presence of Cu^{2+}, Zn^{2+}, and Fe^{2+} accelerated it. The aggregation was triggered extensively by Cu^{2+} (black, Fig. 4) and Zn^{2+} (blue, Fig. 4), but Fe^{2+} (olive, Fig. 4) exhibited a lower propensity for promoting $A\beta_{1-40}$ aggregation than Cu^{2+} and Zn^{2+}. Furthermore, the addition of **PA^{19}fCP** dramatically reduced the build-up of fibrils in the Cu^{2+} induced aggregation (red, Fig. 4) but exhibited very little or almost no effect on the aggregation induced by Zn^{2+} (magenta, Fig. 4) and Fe^{2+} (pink, Fig. 4), respectively. In other words, **PA^{19}fCP** exhibited minor or almost negligible inhibition effects on the Zn^{2+} and Fe^{2+} promoted fibrils. These results indicated the highest affinity of the picolinic moiety present in **PA^{19}fCP** to Cu^{2+} ions. However, it also chelated Zn^{2+} and Fe^{2+} ions with a lower affinity than Cu^{2+} ions.

Investigation of metal binding to PA^{19}fCP by isothermal titration calorimetry (ITC)

Next, to study the interactions of Cu^{2+}, Zn^{2+}, and Fe^{2+} with **PA^{19}fCP**, ITC experiments were performed separately for each metal ion using a Microcal ITC 200 microcalorimeter. The thermodynamic binding parameters associated with the metal–protein interactions can be determined from ITC data.[52,53]

The metal solutions (1.5 mM) were placed in the syringe and the peptide solution (50 μM) in the sample cell. While running the three experiments, all the ITC run parameters and injection parameters were maintained constant to

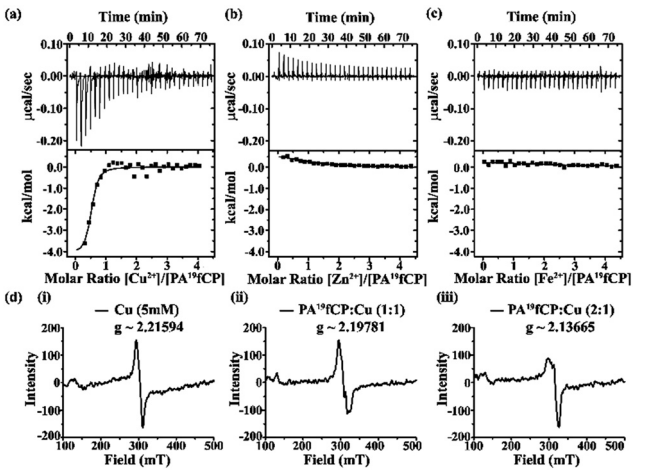

Fig. 5 ITC curves for the binding of (a) Cu^{2+}, (b) Zn^{2+} and (c) Fe^{2+} to **PA^{19}fCP**. The top panel of (a)–(c) represents data obtained for automatic injections after baseline corrections. The bottom panel shows the integrated curve. The experimental points thus obtained were fitted into a sequential two-site binding model after subtraction of the data obtained for the control experiment. (d) ESR spectra of (i) Cu^{2+} alone and in the presence of (ii) 1-fold molar ratio and (iii) 2-fold molar ratio of **PA^{19}fCP**. The representative results out of several independent repeats are shown.

compare the binding interactions properly. During titrations, 1.3 μL of the metal solutions were added from the syringe into the sample cell containing the peptide solution at an interval of 150 s with a stirring speed of 200 rpm. A total of 30 injections were carried out for all the experiments. The titrations were performed at pH 7.4 using Tris-HCl buffer (20 mM) at 27 °C. The top panel of Fig. 5(a)–(c) shows the raw data of heat generation during interactions of **PA^{19}fCP** with Cu^{2+}, Zn^{2+}, and Fe^{2+}, respectively. The experimental points thus obtained were fitted into an integrated curve in the bottom panel using Origin software supplied by Microcal, with the solid line representing the best fit one. The integrated heats of the reaction were plotted against the molar ratios using a two-site sequential binding model after deleting the first titration point. Heats of dilution were determined by titration of metal solutions in the buffer and subtracted from the metal–peptide titration data. Thermodynamic parameters such as binding enthalpy (ΔH, cal mol^{-1}), binding entropy (ΔS, cal mol^{-1} deg^{-1}), binding constant (K), and the number of binding sites (n) were determined by fitting experimental data into a two-site sequential binding model (detailed text in page S19 and S20, ESI†).

It was observed from the ITC raw data that the binding interactions between Cu^{2+} and **PA^{19}fCP** exhibited an exothermic heat event (Fig. 5(a)), while that between Zn^{2+} and **PA^{19}fCP** followed an endothermic event (Fig. 5(b)). However, such interaction for **PA^{19}fCP** binding to Fe^{2+} was negligible (Fig. 5(c)). Hence, **PA^{19}fCP** exhibited a smooth binding isotherm with Cu^{2+}, but not with Zn^{2+} and Fe^{2+}. This result further confirms the binding affinity of **PA^{19}fCP** towards these metal ions, Cu^{2+} exhibiting the highest affinity, followed by Zn^{2+} with Fe^{2+} revealing significantly less or almost no such affinity.

Investigations of Cu-complexation with PA^{19}fCP by electron spin resonance (ESR)

To confirm the binding of Cu(II) to **PA** in **PA^{19}fCP**, an ESR experiment was performed at room temperature. Copper(II) with a $3d^9$ configuration in its ground state is ESR active owing to an unpaired electron, and hence, the effective spin is equal to $S = \frac{1}{2}$. Due to spin–orbit coupling, Zeeman splitting or 'g' factors are shifted from the free-electron value of 2.0023.[54] When the ESR of a Cu^{2+} solution (5 mM) was recorded, it exhibited a strong ESR signal with a g value approximately equal to 2.21594 (Fig. 5d(i)). However, in the presence of 1- and 2-fold molar excesses of **PA^{19}fCP**, ESR scans of the solutions exhibited deformed signals in both cases (Fig. 5d(ii) and (iii)) with g values of 2.19781 and 2.13665, respectively. Thus, the picolinic moiety chelated copper in the presence of both 1- and 2-fold molar excesses of **PA^{19}fCP**. Reduction in ESR signal intensity and deviation in g values of Cu^{2+} solutions of **PA^{19}fCP** from that of only Cu^{2+} solutions suggested the complexation of Cu^{2+} to **PA** in **PA^{19}fCP**. Once the picolinic moiety chelates Cu^{2+} ions, the orientation and geometry around the metal ion undergo modifications, as revealed from the deformation of the ESR signals.

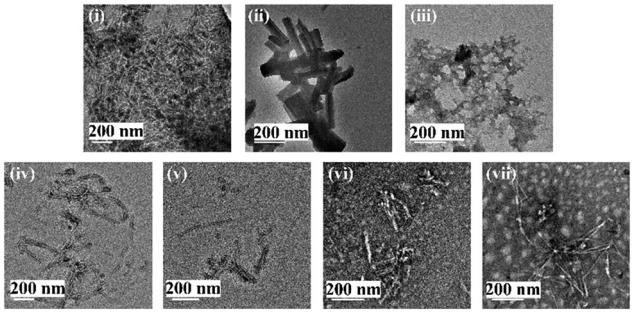

Fig. 6 TEM images of (i) $A\beta_{1-40}$ alone, (ii) $A\beta_{1-40}$ + Cu^{2+}, (iii) $A\beta_{1-40}$ + Cu^{2+} + **PA^{19}fCP**, (iv) $A\beta_{1-40}$ + Zn^{2+}, (v) $A\beta_{1-40}$ + Zn^{2+} + **PA^{19}fCP**, (vi) $A\beta_{1-40}$ + Fe^{2+}, and (vii) $A\beta_{1-40}$ + Fe^{2+} + **PA^{19}fCP** ([$A\beta_{1-40}$] = 40 μM; [M^{2+}] = 40 μM; [**PA^{19}fCP**] = 80 μM). One of the images out of several repeats are presented.

TEM investigations for metal binding to PA^{19}fCP

The impact of **PA^{19}fCP** on metal-induced $A\beta_{1-40}$ aggregation was also monitored by TEM.[39] The TEM images demonstrated the metal chelation by **PA^{19}fCP**, and in fact, **PA^{19}fCP** played an active role in the partial disassembly of $A\beta_{1-40}$ aggregates. All the samples were incubated at 37 °C in PBS at pH 7.4 for 36 h. $A\beta_{1-40}$ alone exhibited a fibril-rich network under TEM (Fig. 6(i)). However, well-organized thick bulky mature fibrils (Fig. 6(ii)) were noted in the presence of Cu^{2+} ions, and some small and thin fibrillar assembly was observed under TEM (Fig. 6(iv) and (vi)) in the presence of Zn^{2+} and Fe^{2+}. On the other hand, the aggregates' morphology altered upon adding PA19fCP into the samples containing $A\beta_{1-40}$ and metal ions. When **PA^{19}fCP** was added to the sample containing $A\beta_{1-40}$ and Cu^{2+}, no such fibrillar assembly was detected; instead, some off-pathway aggregates were observed (Fig. 6(iii)). However, when **PA^{19}fCP** was added separately to the samples containing $A\beta_{1-40}$ with Zn^{2+} and $A\beta_{1-40}$ with Fe^{2+}, some short, thin fibrils appeared (Fig. 6(v) and (vii)). Thus, these TEM results collectively suggested that **PA^{19}fCP** exhibited a significant role in extracting Cu^{2+} ions from Aβ aggregates, thereby perturbing the metal-induced Aβ aggregation pathway. Conversely, the metal extraction efficiency of **PA^{19}fCP** from Aβ aggregates seemed to be intermediate for Zn^{2+} and negligible for Fe^{2+} ions from the TEM images. These results were consistent with those obtained from the ThT fluorescence assay, UV, and ITC studies, strongly indicating that **PA^{19}fCP** can well inhibit, slow down, and alter the copper-induced $A\beta_{1-40}$ aggregation pathway.

Tyrosine intrinsic fluorescence assay to investigate the Cu^{2+}-extraction ability of PA^{19}fCP from Aβ-Cu^{2+} complexes

The results above indicate that PA19fCP exhibits more profound selectivity in chelating copper ions than zinc and

iron. Therefore, focusing primarily on Cu(II) ions, we next investigated the metal extraction ability of **PA^{19}fCP** from Aβ-Cu^{2+} complexes by a tyrosine fluorescence quenching experiment using the inherent Tyr10 fluorescence assay. Aβ-Bound Cu^{2+} gets reduced to Cu^{+} in the presence of bio-reductants and initiates a series of reduction processes, generating reactive oxygen species (ROS) through a Fenton-type reaction.[55,56] Hence, sequestration of copper ions from Aβ-bound copper serves as a promising route for suppressing metal-induced Aβ toxicity. Since Tyr10 in Aβ is located near three histidine residues (His6, His13, and His14), the fluorescence emission intensity of Tyr10 is altered by metal coordination.[57,58] The intrinsic fluorescence of tyrosine in $Aβ_{1–40}$ gets quenched when the Cu^{2+} ion coordinates to the $Aβ_{1–40}$ peptide. Upon sequestration of Cu^{2+} ions with specific chelators, the fluorescence intensity of Tyr10 is regained, exhibiting its characteristic emission peak at 308 nm.[58,59] The magnitude of regaining the fluorescence intensity of Tyr10 signifies the extent of the sequestering ability.

This transformation in Tyr10 intrinsic fluorescence was utilized to investigate the ability of **PA^{19}fCP** to extract Cu^{2+} ions from $Aβ_{1–40}$-Cu^{2+} aggregates. When $Aβ_{1–40}$ (40 μM) was incubated alone in PBS (50 mM, pH 7.4) and then fluorescence was recorded, the emission spectra exhibited the characteristic peak of Tyr10 at 308 nm (black, Fig. 7(a) and (b)). Upon adding a 40 μM concentration of Cu^{2+} ions into the $Aβ_{1–40}$ solution, the fluorescence intensity decreased significantly owing to the quenching of Tyr10 (red, Fig. 7(a) and (b)). The fluorescence quenching of Tyr10 occurs rapidly due to the formation of the $Aβ_{1–40}$-Cu^{2+} complex with the three histidine moieties. Remarkably, the quenched intrinsic fluorescence of Tyr10 regained rapidly upon addition of **PA^{19}fCP** (80 μM) to the incubated $Aβ_{1–40}$-Cu^{2+} solution (blue, Fig. 7(a) and (b)). In other words, the presence of **PA^{19}fCP** could restore the fluorescence of Tyr10 up to 84.3% (Fig. 7(b)). This observation signifies the ability of **PA^{19}fCP** to chelate copper out of the $Aβ_{1–40}$-Cu^{2+} complex, thereby preventing the redox cycle.

Förster resonance energy transfer (FRET) assay for studying interaction between $Aβ_{1–40}$ and CPs

Förster resonance energy transfer (FRET) is a non-radiative process of energy transfer from an excited fluorophore (the donor) to a proximal ground state fluorophore (the acceptor) through a long-range dipole–dipole coupling mechanism.[60] It is a distance-dependent physical process that can provide an insight into the energy transfer process at a molecular proximity of 10–100 Å.[61] The efficiency of energy transfers between the FRET donor and the FRET acceptor is highly dependent on several factors, including the extent of spectral overlap, the relative orientation of the transition dipoles, and primarily, the distance between the donor and the acceptor molecules.[62] The FRET assay is a promising tool for characterizing protein–protein, DNA–protein, and lipid–protein interactions both *in vitro* and *in vivo*.[63] Therefore, before the FRET assay, choosing a suitable FRET pair is of paramount importance. In our study, we have chosen Rhodamine B (RhB) and 5(6)-fluorescein-isothiocyanate (FITC) as FRET pairs, with the former behaving as a FRET acceptor and the latter as a FRET donor. These xanthene compounds are often paired for FRET-based experiments because of efficient energy transfer between Rhodamine labels and fluorescein derivatives.[64] To gain insight into the interactions between the designed cyclic peptides and $Aβ_{1–40}$, we performed FRET assays at physiological pH *in vitro*. For this purpose, considering the characteristics of both **PA^{19}fCP** and **^{19}fCP**, we designed and synthesized another cyclic peptidomimetic, namely **PA^{19}fCP-Fl**, attaching fluorescein iso-thiocyanate (FITC, Fl) as a fluorophore at the side-chain of lysine towards the C-terminus (Fig. 1). A partial sequence

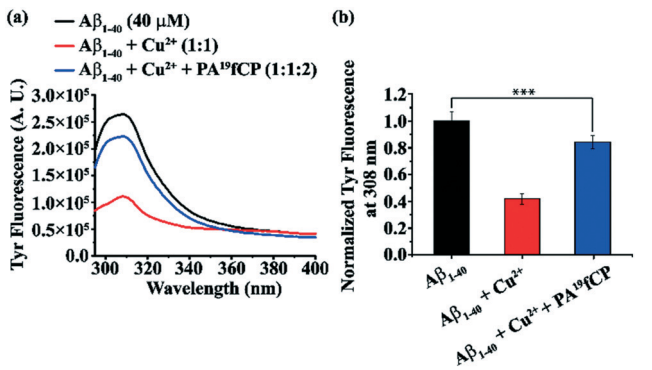

Fig. 7 (a) Tyr10 fluorescence of $Aβ_{1–40}$ (40 μM) alone (black) and in the presence of Cu^{2+} ions (1 : 1) (red) and Cu^{2+} ions and **PA^{19}fCP** (1 : 1 : 2) (blue) in PBS buffer (50 mM, pH 7.4), (b) bar diagram of Tyr10 normalized fluorescence intensity (NFI) of $Aβ_{1–40}$ (40 μM) alone (black) and in the presence of Cu^{2+} ions (1 : 1) (red) and Cu^{2+} ions and **PA^{19}fCP** (1 : 1 : 2) (blue) in PBS buffer (50 mM, pH 7.4). The presented results are the average of three independent experiments. The error bar corresponds to the standard deviation (SD) of the value (***$p \leq 0.001$).

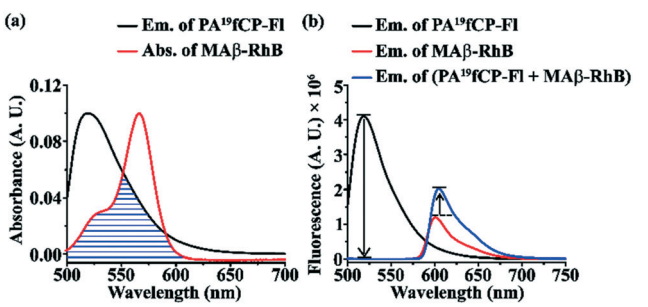

Fig. 8 (a) Overlap of the emission spectrum of donor peptide **PA^{19}fCP-Fl** (black) and the absorbance spectrum of acceptor peptide **MAβ-RhB** (red), (b) fluorescence emission spectra of donor peptide **PA^{19}fCP-Fl** (black), acceptor peptide **MAβ-RhB** (red) and a mixture of both donor and acceptor peptides (**PA^{19}fCP-Fl** + **MAβ-RhB**) (blue). Peptides **PA^{19}fCP-Fl** and (**PA^{19}fCP-Fl** + **MAβ-RhB**) were excited at 492 nm, whereas peptide **MAβ-RhB** was excited at 567 nm. Spectra were recorded with 20 μM solutions of the peptides in PBS (50 mM, pH 7.4) after 24 h of incubation of the peptide samples. The representative results out of several independent repeats are presented.

of $A\beta_{1-40}$ peptide ($A\beta_{9-21}$), a model Aβ peptide, namely **MAβ-RhB**, was also synthesized, attaching Rhodamine B (RhB) as a fluorophore at the C-terminus (Fig. 1). We prepared ~20 μM concentration solutions of both fluorophoric peptides, **PA^{19}fCP-Fl** and **MAβ-RhB** in PBS (50 mM at pH 7.4). All the three peptide samples, **PA^{19}fCP-Fl**, **MAβ-RhB**, and (**PA^{19}fCP-Fl** + **MAβ-RhB**, mixed in a 1:1 molar ratio), were kept in incubation at 37 °C. The UV-visible and fluorescence spectra of the individual donor and acceptor revealed that the emission spectra of FITC in peptide **PA^{19}fCP-Fl** (FRET donor) (black, Fig. 8(a)) overlapped significantly with the absorption spectra of Rhodamine B in peptide **MAβ-RhB** (FRET acceptor) (red, Fig. 8(a)). In other words, both the donor and acceptor peptides have fulfilled the criteria for exhibiting significant energy transfer.

After 24 h incubation at 37 °C, the fluorescence intensity of the donor (FITC in peptide **PA^{19}fCP-Fl** + **MAβ-RhB**, λ_{max}^{Em} = 518 nm, blue, Fig. 8(b)) decreased significantly compared with that of the donor alone (FITC in peptide **PA^{19}fCP-Fl**, λ_{max}^{Em} = 518 nm, black, Fig. 8(b)) when excited at the maximum absorbance of the donor (λ_{max}^{Abs} = 492 nm). Simultaneously, the fluorescence intensity of the acceptor (RhB in peptide **PA^{19}fCP-Fl** + **MAβ-RhB**, λ_{max}^{Em} = 604 nm, blue, Fig. 8(b)) increased almost 1.6 times than that of the acceptor alone (RhB in peptide **MAβ-RhB**, λ_{max}^{Em} = 601 nm, red, Fig. 8(b)). These variations in fluorescence intensities provided clear evidence of the FRET from the donor (FITC in peptide **PA^{19}fCP-Fl**) to the acceptor (RhB in peptide **MAβ-RhB**). This energy transfer process provided an insight into the molecular interactions between the cyclic peptide and model Aβ peptide. Since the cyclic peptide was designed to maintain sequence homology with the recognizing motif of $A\beta_{1-40}$, it is expected that the former would recognize, bind, and interact with the latter, evident from the FRET assay.

Investigation of toxicity, cell-internalization, and co-localization of FRET pairs in the cell

The above FRET assay indicated that peptide **PA^{19}fCP-Fl** could bind efficiently to **MAβ-RhB**, evident from the energy transfer process. However, to know the physiological relevance of the **CP**s, their cell internalization capabilities and toxicity are of paramount importance. Therefore, we checked the toxicity and cell penetration abilities of **PA^{19}fCP-Fl** and **MAβ-RhB**. The MTT assay of both peptides in the mouse neuronal cell line (Neuro2a) did not show cellular toxicity even at higher concentrations. The concentrations of the peptides responsible for the viability of 50% of the treated cells (IC_{50}) were ~200 μM and ~150 μM for **PA^{19}fCP-Fl** and **MAβ-RhB**, respectively (Fig. 9(a) and (b)).

To check the internalization of peptides inside cells, **PA^{19}fCP-Fl** and **MAβ-RhB** were further treated in Neuro2a cells at 100 μM concentration. Cellular imaging also showed green and red fluorescence inside cells for **PA^{19}fCP-Fl** and **MAβ-RhB**, respectively, which indicated that both peptides were present in the cell membrane and cytoplasm

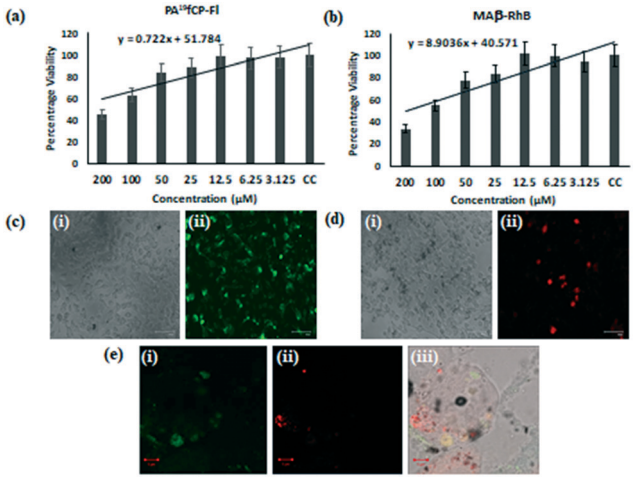

Fig. 9 (a) and (b) Cytotoxicity analyses of **PA^{19}fCP-Fl** and **MAβ-RhB**, respectively, in Neuro2a cells post 24 h. IC_{50} values were calculated as per the equation derived from linear regression analyses. (c)–(e) Fluorescence images showing cell penetration of (c) **PA^{19}fCP-Fl** and (d) **MAβ-RhB** and (e) co-localization of the FRET pair inside Neuro2a cells; (c) (i) bright-field and (ii) dark-field images of **PA^{19}fCP-Fl** green fluorescence inside cells; (d) (i) bright-field and (ii) dark-field images of **MAβ-RhB** red fluorescence inside cells at 20× magnification; (e) confocal images of Neuro2a cells in 63× magnification to check co-localization of the FRET pair inside cells treated with both **PA^{19}fCP-Fl** and **MAβ-RhB**, individual dark-field images with (i) green and (ii) red channels were captured separately, (iii) merged image with yellow color highlighting co-localization of the FRET pair. The representative images out of several independent repeats are presented.

(Fig. 9(c) and (d) respectively). Further, the plausible interaction between the FRET pair inside cells was analyzed by confocal microscopy. At 63× magnification, the imaging revealed a noticeable change in color to yellow when individual dark-field images were merged. The yellow color confirmed the co-localization of **PA19fCP-Fl** and **MAβ-RhB** in the same area in the cell (Fig. 9(e)). This result indicates a possibility of interaction between two peptides at a cellular level.

Preliminary investigation on the mechanism of inhibition of $A\beta_{1-40}$ by CPs

To gain mechanistic insight into the inhibitory action of the CPs on $A\beta_{1-40}$ aggregation, we studied the changes in the dimensions of the aggregated species of $A\beta_{1-40}$ (40 μM) alone as well as in the presence of 2 equivalents of CPs (80 μM) with time by using dynamic light scattering (DLS). We have considered only one cyclic peptide (**PA^{19}fCP**) for the mechanism study due to its better inhibitory efficacy than **^{19}fCP**. When incubated alone at pH 7.4 and 37 °C, the hydrodynamic diameter (d) of $A\beta_{1-40}$ particles increased gradually from several nanometers (monomers) to several micrometers *via* intermediate oligomer formation of size distribution ranging from 100–1000 nm. Increasing the incubation period gradually, the sizes of the particles increased along with the broadening in size distribution,

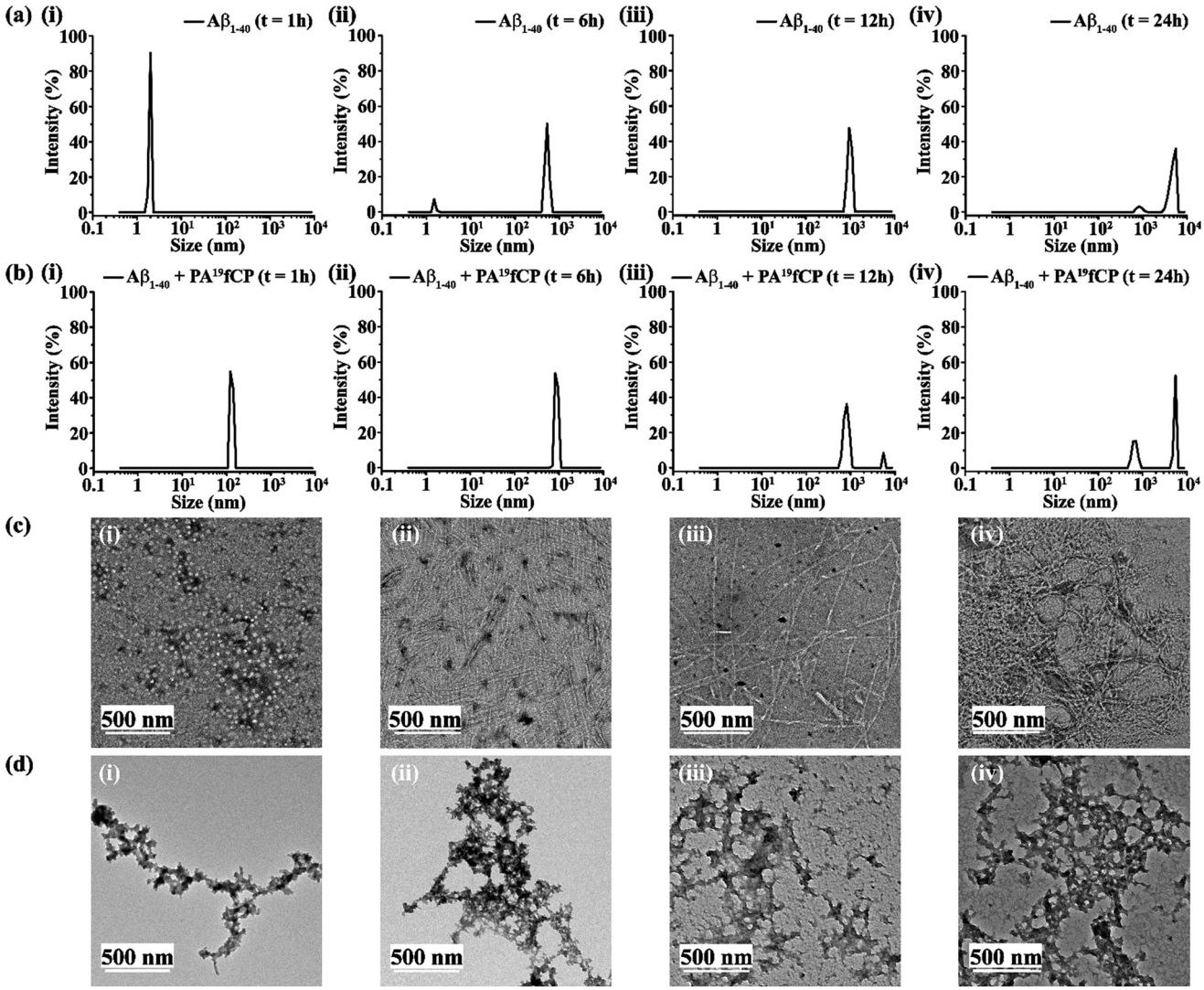

Fig. 10 DLS results showing the size distribution of $A\beta_{1-40}$ (40 μM) (a) alone at (i) 1 h, (ii) 6 h, (iii) 12 h and (iv) 24 h of incubation as well as (b) in the presence of 2 equivalents of **PA^{19}fCP** at (i) 1 h, (ii) 6 h, (iii) 12 h and (iv) 24 h of incubation of the peptide samples. TEM images of $A\beta_{1-40}$ (40 μM) (c) alone at (i) 1 h, (ii) 6 h, (iii) 12 h and (iv) 24 h of incubation as well as (d) in the presence of 2 equivalents of **PA^{19}fCP** at (i) 1 h, (ii) 6 h, (iii) 12 h and (iv) 24 h of incubation of the peptide samples. The scale bars for (c) and (d) are 500 nm. The representative results out of several independent repeats are presented.

indicating the formation of fibrillar species (Fig. 10(a) (i)–(iv)). On the contrary, when $A\beta_{1-40}$ was incubated for one hour in the presence of **PA^{19}fCP**, some aggregated species with size distribution centered at 100 nm appeared instantly (Fig. 10(b) (i)), possibly through a pathway different from its native aggregation route. Further incubation increased the growth of the aggregated species exhibiting size distributions from 1000 to 10 000 nm (Fig. 10(b) (ii)–(iv)). This drastic variation in the pattern of size distributions suggests that **PA^{19}fCP** alters the aggregation pathway of $A\beta_{1-40}$ and proceeds towards an off-pathway aggregation route.[18]

A TEM experiment was performed at different time intervals to gain further evidence of the inhibition process and investigate the morphological features of the different species formed. When incubated alone at pH 7.4 and 37 °C, $A\beta_{1-40}$ displayed monomeric (Fig. 10(c) (i)) and oligomeric (Fig. 10(c) (ii)) species under TEM after 1 h and 6 h of incubation, respectively. Extending the incubation period up to 12 h resulted in the formation of long and thin fibrils as detected under TEM (Fig. 10(c) (iii)). Finally, 24 h of incubation of the $A\beta_{1-40}$ sample generated a dense network of fibrillar morphology as observed under TEM (Fig. 10(c) (iv)).

In contrast, when incubated with **PA^{19}fCP**, the morphological species observed under TEM were dramatically different from native $A\beta_{1-40}$. For $A\beta_{1-40}$, in the presence of **PA^{19}fCP**, instead of the fibrillar morphology, some inhibitor-embedded off-pathway aggregated species formed instantly and predominantly. These species assembled gradually with larger particles under physiological conditions, which resulted in their increased aggregation with time ((Fig. 10(d) (i)–(iv)).

Thus, the morphological features observed under TEM analysis were in excellent and convincing agreement with the DLS results. The DLS and TEM results collectively indicate that the presence of **PA^{19}fCP** diverts the native aggregation pathway of Aβ_{1-40} and instead leads to the formation of non-toxic off-pathway species that cannot proceed to amyloid fibrils.

Vesicle leakage assay

Aβ_{1-40} self-assembly generates both 'on-pathway' oligomeric intermediate species that proceed to amyloid fibers or sometimes 'off-pathway' species independent of fiber formation.[65] Aβ_{1-40} soluble oligomers are more toxic than mature amyloid fibrils as the former cause cell membrane damage.[66] Ramamoorthy *et al.* demonstrated that such toxicity arises *via* a two-step mechanism. In the first step, small pores are formed in the membrane, while in the second step, the membrane is destroyed with the detergent-like mechanism.[67]

Our experimental findings indicated that the Aβ_{1-40} aggregation pathway resulted in the formation of off-pathway species in the presence of **PA^{19}fCP**.

We performed a dye leakage assay to investigate the membrane damage ability of these species. We initially prepared carboxyfluorescein dye entrapped large unilamellar vesicles[68] (LUVs; detailed text on pages S22 and S23, ESI†). TEM images of LUVs revealed their spherical shapes and uniform sizes (Fig. 11(a) (i) and (ii)). We prepared three sets of samples to perform the vesicle leakage assay, including the untreated LUV (LUV without any peptide) as the control. Next, two peptide solutions, one Aβ_{1-40} solution (40 μM) and the other Aβ_{1-40} mixed with **PA^{19}fCP** in a molar ratio of 1 : 2

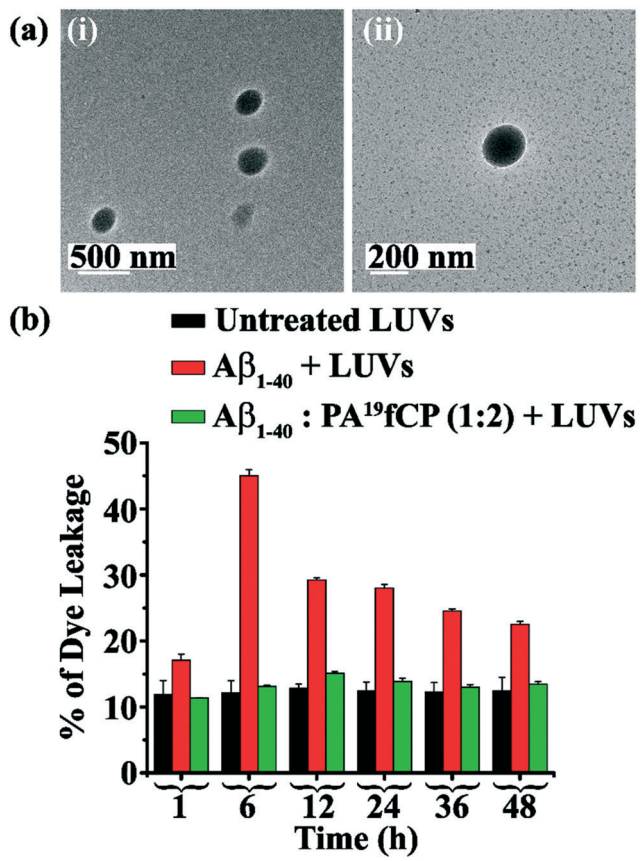

Fig. 11 (a) TEM images (i and ii) of the LUVs (1 mM) in PBS buffer (50 mM). Images were captured after the immediate preparation of the vesicles. Scale bars for (i) and (ii) are indicated as 500 nm and 200 nm, respectively; representative images out of several independent repeats are presented. (b) The emission of carboxyfluorescein dye from large unilamellar vesicles (LUVs) shows Aβ_{1-40} on the LUVs with time and % of dye leakage in the absence and presence of **PA^{19}fCP** from 1 h to 48 h. The presented results are an average of three independent experiments. Error bars indicate standard deviations.

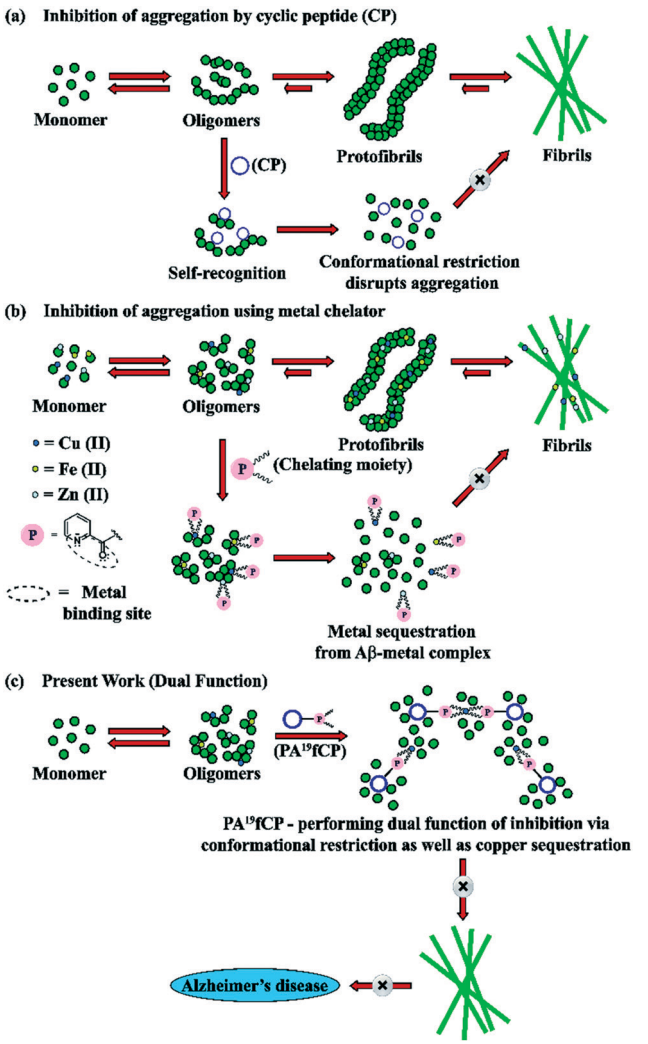

Scheme 1 Proposed hypothesis for (a) inhibition of Aβ_{1-40} aggregation by the conformational restriction imposed by the cyclic peptide, (b) inhibition of Aβ_{1-40} aggregation by metal sequestration using a specific metal chelator, and (c) dual function of inhibition of aggregation as well as metal sequestration from the Aβ_{1-40}-metal complex by **PA^{19}fCP**. (The picolinic moiety in **PA^{19}fCP** served as a specific metal chelator).

were prepared in PBS (50 mM). Then 25 μL of the dye-loaded LUVs and 50 μL each of the peptide solutions were added separately and diluted up to 1000 μL to obtain a final concentration of 50 μM for the lipid solution and 2.5 μM for $A\beta_{1-40}$ solution, with the peptide and the lipid maintaining a molar ratio of 1 : 20. All the samples were incubated at 37 °C, and dye leakage studies were performed at different time intervals.

The most rapid and prominent increment of carboxyfluorescein dye leakage occurred from the LUV treated with the 6 h old incubated sample of $A\beta_{1-40}$ (red at 6 h, Fig. 11(b)). This dye leakage indicates the formation of highly toxic oligomeric intermediates, which cause membrane disruption by pore formation on the LUV, leading to pronounced dye leakage from the LUV. However, after 6 h, the percentage of dye leakage from the $A\beta_{1-40}$ sample decreased gradually upon extending the incubation time from 12 h to 48 h (red, Fig. 11(b)). In other words, from 12 h onwards, the incubated $A\beta_{1-40}$ sample forms fibrillar species, which are relatively non-toxic, as they do not cause significant pore formation on the LUV, as is evident from the extent of dye leakage. On the other hand, incubation of $A\beta_{1-40}$ in the presence of **PA^{19}fCP** up to 48 h resulted in no significant change in the percentage of dye leakage (green, Fig. 11(b)). The corresponding fluorescence intensity was as low as the untreated LUV (black, Fig. 11(b)). These results indicate that **PA^{19}fCP** prohibited pore formation on the treated LUV, and no evidence of toxic pore-forming species was detected even after 48 h of incubation of the peptide samples. Thus, the off-pathway species generated when $A\beta_{1-40}$ was co-incubated with **PA^{19}fCP** do not cause membrane disruption or pore formation; therefore, they are non-toxic, as further confirmed by cytotoxicity results *vide supra*.

Conclusions

In summary, we have designed, synthesized, and characterized two head-to-tail cyclic peptides (**PA^{19}fCP** and **^{19}fCP**) with and without attaching a metal-binding moiety, picolinic acid, into the peptide sequence as well as a linear peptide for use as a control peptide. We have demonstrated the efficacies of the synthesized peptides to inhibit Aβ fibrillogenesis under physiological conditions using different biophysical tools. We emphasized two comparisons, comparing the inhibitory potencies of the cyclic peptide *versus* its linear counterpart and comparing two cyclic peptides (**PA^{19}fCP** and **^{19}fCP**). It was noted that cyclic peptides are far better amyloid aggregation inhibitors than their linear analogs. Notably, a two-fold molar excess of the cyclic peptides dramatically reduced Aβ aggregation compared to the linear peptide.

Further, **PA^{19}fCP** was a better inhibitor of $A\beta_{1-40}$ aggregation than **^{19}fCP**, owing to the picolinic acid. The picolinic acid-containing cyclic peptide (**PA^{19}fCP**) was designed to inhibit Aβ aggregation by the synergistic action of conformational restriction and metal chelation (Scheme 1). Indeed, it behaves as a metal chelator and exhibited significant perturbation against metal-induced Aβ aggregation, as confirmed by the ThT fluorescence assay, isothermal titration calorimetry measurements, electron spin resonance experiments, TEM, and tyrosine intrinsic fluorescence assay. The picolinic acid moiety exhibited profound selectivity in sequestration of metal ions from the Aβ-metal complex, showing the highest affinity for Cu(II), followed by Zn(II) and then Fe(II) ions.

A preliminary mechanism study was performed using a combination of DLS, TEM, and the large unilamellar vesicle leakage assay. The cyclic peptides prevented the growth of amyloid fibrils by altering the toxic pathway; instead, their presence with $A\beta_{1-40}$ leads the aggregation to an off-pathway route generating some non-toxic species as confirmed by DLS, TEM, the vesicle leakage assay, and MTT assay. The molecular-level interaction between **PA^{19}fCP** and a model Aβ peptide was confirmed by FRET phenomena between the fluorescently labeled analogs, **PA^{19}fCP-Fl** and **MAβ-RhB**. Cell penetration and co-localization in the same region inside the cells were also confirmed using **PA^{19}fCP-Fl** and **MAβ-RhB**. The association of such a metal chelator with further modifications of cyclic peptides may be a promising approach for developing anti-Alzheimer's agents. A similar idea may be used for drug design against other amyloidoses. Nevertheless, the present study sheds light on the aggregation process and ways of its perturbation.

Conflicts of interest

There is no conflict to declare.

Acknowledgements

We are thankful to CIF, IIT Guwahati for ITC, ESR and TEM facilities and the Department of Chemistry (COE-FAST and FIST), IIT Guwahati for NMR and HRMS facilities. We are thankful to the Department of Biotechnology (BT/PR16164/NER/95/88/2015 and BT/PR29978/MED/30/2037/2018) for the financial support.

Notes and references

1 F. Chiti and C. M. Dobson, *Annu. Rev. Biochem.*, 2006, **75**, 333–366.
2 S. A. Funke and D. Willbold, *Curr. Pharm. Des.*, 2012, **18**, 755–767.
3 K. Rajasekhar, M. Chakrabarti and T. Govindaraju, *Chem. Commun.*, 2015, **51**, 13434–13450.
4 T. P. J. Knowles, M. Vendruscolo and C. M. Dobson, *Nat. Rev. Mol. Cell Biol.*, 2014, **15**, 384–396.
5 D. J. Selkoe, *Physiol. Rev.*, 2001, **81**, 741–766.
6 D. J. Selkoe, *Nature*, 2003, **426**, 900–904.
7 L. O. Tjernberg, J. Naslund, F. Lindqvist, J. Johansson, A. R. Karlstrom, J. Thyberg, L. Terenius and C. Nordstedt, *J. Biol. Chem.*, 1996, **271**, 8545–8548.

8 C. Soto, E. M. Sigurdsson, L. Morelli, R. A. Kumar, E. M. Castano and B. Frangione, *Nat. Med.*, 1998, **4**, 822–826.
9 A. Paul, K. C. Nadimpally, T. Mondal, K. Thalluri and B. Mandal, *Chem. Commun.*, 2015, **51**, 2245–2248.
10 H. F. Ji and H. Y. Zhang, *Acta Pharmacol. Sin.*, 2008, **29**, 143–151.
11 K. Pagano, S. Tomaselli, H. Molinari and L. Ragona, *Front. Neurosci.*, 2020, **14**, 619667.
12 A. Pithadia, J. R. Brender, C. A. Fierke and A. Ramamoorthy, *J. Diabetes Res.*, 2015, **2016**, 2046327.
13 C. Terry, *Curr. Res. Biotechnol.*, 2020, **2**, 131–144.
14 L. Ma, C. Yang, J. Zheng, Y. Chen, Y. Xiao and K. Huang, *Eur. J. Med. Chem.*, 2020, **192**, 112197.
15 K. W. Menting and J. A. H. R. Claassen, *Front. Aging Neurosci.*, 2014, **6**, 1–9.
16 J. J. Chen, W. Qian, K. Biswas, C. Yuan, A. Amegadzie, Q. Liu, T. Nixey, J. Zhu, M. Ncube, R. M. Rzasa, F. Chavez Jr, N. Chen, F. DeMorin, S. Rumfelt, C. M. Tegley, J. R. Allen, S. Hitchcock, R. Hungate, M. D. Bartberger, L. Zalameda, Y. Liu, J. D. McCarter, J. Zhang, L. Zhu, S. Babu-Khan, Y. Luo, J. Bradley, P. H. Wen, D. L. Reid, F. Koegler, C. Dean Jr, D. Hickman, T. L. Correll, T. Williamson and S. Wood, *Bioorg. Med. Chem. Lett.*, 2013, **23**, 6447–6454.
17 T. Arai, T. Araya, D. Sasaki, A. Taniguchi, T. Sato, Y. Sohma and M. Kanai, *Angew. Chem., Int. Ed.*, 2014, **53**, 8236–8239.
18 T. Arai, D. Sasaki, T. Araya, T. Sato, Y. Sohma and M. Kanai, *ChemBioChem*, 2014, **15**, 2577–2583.
19 J. Luo and J. P. Abrahams, *Chem. – Eur. J.*, 2014, **20**, 2410–2419.
20 A. Zorzi, K. Deyle and C. Heinis, *Curr. Opin. Chem. Biol.*, 2017, **38**, 24–29.
21 A. T. Petkova, Y. Ishii, J. J. Balbach, O. N. Antzutkin, R. D. Leapman, F. Delaglio and R. Tycko, *Proc. Natl. Acad. Sci. U. S. A.*, 2002, **99**, 16742–16747.
22 J. Ghanta, C. L. Shen, L. L. Kiessling and R. M. Murphy, *J. Biol. Chem.*, 1996, **271**, 29525–29528.
23 C. Soto, M. S. Kindy, M. Baumann and B. Frangione, *Biochem. Biophys. Res. Commun.*, 1996, **226**, 672–680.
24 A. Kapurniotu, A. Buck, M. Weber, A. Schmauder, T. Hirsch, J. Bernhagen and M. T. Nossol, *Chem. Biol.*, 2003, **10**, 149–159.
25 A. K. Yudin, *Chem. Sci.*, 2015, **6**, 30–49.
26 M. Richman, S. Wilk, M. Chemerovski, S. K. T. S. Warmlander, A. Wahlstrom, A. Graslund and S. Rahimipour, *J. Am. Chem. Soc.*, 2013, **135**, 3474–3484.
27 E. Karran, M. Mercken and B. D. Strooper, *Nat. Rev.*, 2011, **10**, 698–712.
28 E. Y. Hayden and D. B. Teplow, *Alzheimer's Res. Ther.*, 2013, **5**, 60.
29 E. N. Cline, M. A. Bicca, K. L. Viola and W. L. Klein, *J. Alzheimer's Dis.*, 2018, **64**, S567–S610.
30 M. F. Sciacca, F. Lolicato, C. Tempra, F. Scollo, B. R. Sahoo, M. D. Watson, S. G. Vinuales, D. Milardi, A. Raudino, J. C. Lee, A. Ramamoorthy and C. L. Rosa, *ACS Chem. Neurosci.*, 2020, **11**(24), 4336–4350.
31 A. D'Anneo, C. C. Bavisotto, A. M. Gammazza, L. Paladino, D. Carlisi, F. Cappello, E. C. de Macario, A. J. L. Macario and M. Lauricella, *Cell Stress Chaperones*, 2020, **25**, 805–820.
32 Y. Liu, M. Nguyen, A. Robert and B. Meunier, *Acc. Chem. Res.*, 2019, **52**, 2026–2035.
33 D. G. Smith, R. Cappai and K. J. Barnham, *Biochim. Biophys. Acta*, 2007, **1768**, 1976–1990.
34 M. A. Lovell, J. D. Robertson, W. J. Teesdale, J. L. Campbell and W. R. Markesbery, *J. Neurol. Sci.*, 1998, **158**, 47–52.
35 M. G. Savelieff, S. Lee, Y. Liu and M. H. Lim, *ACS Chem. Biol.*, 2013, **8**, 856–865.
36 B. R. Sahoo, W. Liang, W. J. Tang and A. Ramamoorthy, *bioRxiv*, DOI: **10.1101/2020.04.23.057505**.
37 S. Y. Chen, Y. Chen, Y. P. Li, S. H. Chen, J. H. Tan, T. M. Ou, L. Q. Gu and Z. S. Huang, *Bioorg. Med. Chem.*, 2011, **19**, 5596–5604.
38 K. E. S. Matlack, D. F. Tardiff, P. Narayan, S. Hamamichi, K. A. Caldwell, G. A. Caldwell and S. Lindquist, *Proc. Natl. Acad. Sci. U. S. A.*, 2014, **111**(11), 4013–4018.
39 A. M. Mancino, S. S. Hindo, A. Kochi and M. H. Lim, *Inorg. Chem.*, 2009, **48**, 9596–9598.
40 C. Lu, Y. Guo, J. Yan, Z. Luo, H. B. Luo, M. Yan, L. Huang and X. Li, *J. Med. Chem.*, 2013, **56**, 5843–5859.
41 A. K. Sharma, J. Kim, J. T. Prior, N. J. Hawco, N. P. Rath, J. Kim and L. M. Mirica, *Inorg. Chem.*, 2014, **53**, 11367–11376.
42 A. Robert, Y. Liu, M. Nguyen and B. Meunier, *Acc. Chem. Res.*, 2015, **48**, 1332–1339.
43 G. W. Evans, *Life Chem. Rep.*, 1982, **1**, 57–67.
44 R. S. Grant, S. E. Coggan and G. A. Smythe, *Int. J. Tryptophan Res.*, 2009, **2**, 71–79.
45 J. A. Fernandez-Pol, D. J. Klos and P. D. Hamilton, *Anticancer Res.*, 2001, **21**, 3773–3776.
46 R. R. Pulimamidi, R. Nomula, R. Pallepogu and H. Shaik, *Eur. J. Med. Chem.*, 2014, **79**, 117–127.
47 M. C. Alcaro, G. Sabatino, J. Uziel, M. Chelli, M. Ginanneschi, P. Rovero and A. M. Papini, *J. Pept. Sci.*, 2004, **10**, 218–228.
48 R. J. Chalifour, R. W. McLaughlin, L. Lavoie, C. Morissette, N. Tremblay, M. Boule, P. Sarazin, D. Stea, D. Lacombe, P. Tremblay and F. Gervais, *J. Biol. Chem.*, 2003, **278**, 34874–34881.
49 (*a*) M. R. Nilsson, *Methods*, 2004, **34**, 151–160; (*b*) P. Walsh, J. Yau, K. Simonetti and S. Sharpe, *Biochemistry*, 2009, **48**, 5779–5781.
50 C. Wu, J. Scott and J. E. Shea, *Biophys. J.*, 2012, **103**, 550–557.
51 W. H. Wu, P. Lei, Q. Liu, J. Hu, A. P. Gunn, M. S. Chen, Y. F. Rui, X. Y. Su, Z. P. Xie, Y. F. Zhao, A. I. Bush and Y. M. Li, *J. Biol. Chem.*, 2008, **283**, 31657–31664.
52 T. K. Dam, M. Torres, C. F. Brewer and A. Casadevall, *J. Biol. Chem.*, 2008, **283**, 31366–31370.
53 C. A. Brautigam, *Methods*, 2015, **76**, 124–136.
54 (*a*) M. Valko, P. Pelikan, S. Biskupic and M. Mazur, *Chem. Pap.*, 1990, **44**(6), 805–813; (*b*) Z. Yang, M. R. Kurpiewski, M. Ji, J. E. Townsend, P. Mehta, L. J. Jacobson and S. Saxena, *Proc. Natl. Acad. Sci. U. S. A.*, 2012, **109**(17), E993–E1000.

55 F. Arrigoni, T. Prosdocimi, L. Mollica, L. De Gioia, G. Zampella and L. Bertini, *Metallomics*, 2018, **10**, 1618–1630.
56 L. M. F. Gomes, A. Mahammed, K. E. Prosser, J. R. Smith, M. A. Silverman, C. J. Walsby, Z. Gross and T. Storr, *Chem. Sci.*, 2019, **10**, 1634–1643.
57 N. C. Maiti, D. Jiang, A. J. Wain, S. Patel, K. L. Dinh and F. Zhou, *J. Phys. Chem. B*, 2008, **112**, 8406–8411.
58 B. Muthuraj, S. Layek, S. N. Balaji, V. Trivedi and P. K. Iyer, *ACS Chem. Neurosci.*, 2015, **6**, 1880–1891.
59 R. Roy, K. Pradhan, J. Khan, G. Das, N. Mukherjee, D. Das and S. Ghosh, *ACS Omega*, 2020, **5**, 18628–18641.
60 J. R. Lakowicz, *Principles of Fluorescence Spectroscopy*, Kluwer/Plenum, New York, 2nd edn, 1999.
61 R. B. Sekar and A. Periasamy, *J. Cell Biol.*, 2003, **160**, 629–633.
62 K. E. Sapsford, L. Berti and I. L. Medintz, *Angew. Chem., Int. Ed.*, 2006, **45**, 4562–4589.
63 Y. Sun, C. Rombola, V. Jyothikumar and A. Periasamy, *Cytometry, Part A*, 2013, **83**, 780–793.
64 L. D. Lavis and R. T. Raines, *ACS Chem. Biol.*, 2008, **3**, 142–155.
65 J. R. Brender, E. L. Lee, M. A. Cavitt, A. Gafni, D. G. Steel and A. Ramamoorthy, *J. Am. Chem. Soc.*, 2008, **130**, 6424–6429.
66 P. Cao, *et al.*, *Proc. Natl. Acad. Sci. U. S. A.*, 2013, **110**, 19279–19284.
67 M. F. M. Sciacca, S. A. Kotler, J. R. Brender, J. Chen, D. Lee and A. Ramamoorthy, *Biophys. J.*, 2012, **103**, 702–710.
68 (*a*) T. L. Williams, I. J. Day and L. C. Serpell, *Langmuir*, 2010, **26**, 17260–17268; (*b*) M. Traikia, *et al.*, *Eur. Biophys. J.*, 2000, **29**, 184–195.

